Supplementary information for

Leveraging the Redox Activities of Cerium and Dibenzotetrathiafulvalene to Discover a Photo-Responsive Magnetic Material

Himanshu Gupta,[a] Ethan P. Shapera,[b] Xiaojuan Yu,[b] Xiaoyu Wang,[b] Patrick W. Smith,[c] Pragati Pandey,[d] Michael R. Gau,[a] Stefan G. Minasian,*[c] Eva Zurek,*[b] Jochen Autschbach,*[b] James M. Kikkawa,*[e] Eric J. Schelter*[a,f,g]

[a]VLEST, Department of Chemistry, University of Pennsylvania, Philadelphia, PA 19104, USA
[b]Department of Chemistry, University of Buffalo, State University of New York, Buffalo, NY 14260, USA
[c]Chemical Sciences Division, Lawrence Berkeley National Laboratory, Berkeley, CA 94720, USA
[d] Institut des Sciences et Ingénierie Chimiques, École Polytechnique Fédérale de Lausanne (EPFL), CH-1015 Lausanne, Switzerland
[e]Department of Physics and Astronomy, University of Pennsylvania, Philadelphia, PA 19104, USA
[f]Department of Earth and Environmental Science, University of Pennsylvania, Philadelphia, PA 19104, US
[g]Department of Chemical and Biomolecular Engineering, University of Pennsylvania, Philadelphia, PA 19104, USA

*Email: ezurek@buffalo.edu, jochena@buffalo.edu, sgminasian@lbl.gov, kikkawa@physics.upenn.edu, schelter@sas.upenn.edu

Table of Contents:

General Methods and Materials:

All synthetic work and manipulations were performed under aerobic conditions. All glassware were oven-dried at 150 ºC overnight prior to use. Elemental analyses were performed on a Costech ECS 4010 analyzer at the University of Pennsylvania. Carbon tetrachloride, acetonitrile, chloroform and ethanol were purchased from Fisher Scientific and used without further purification. Dibenzotetrathiafulvalene (DBTTF) and $CeCl_3$ were purchased from Sigma Aldrich and used as received. $(NBu_4)_2[CeCl_6]$ was prepared as previously described.[1]

IR Spectroscopy:

FT-IR Spectroscopy data of DBTTF and **1** was collected on a Bruker Invenio-S FT-IR spectrometer. A KBr mixture of the compound was finely ground and pressed with a pellet press to create homogeneous circular pellets, and the pellets were transferred to the spectrometer for measurement.

Electronic Absorption Spectroscopy:

Solution UV-Visible spectra were obtained using a Perkin Elmer 905 UV-Vis-NIR spectrophotometer in absorption mode, and solid-state data were taken in transmission mode on microcrystalline powder. Methanol solutions of known concentration of analyte were prepared on the benchtop and transferred to a quartz cell sealed with a screw cap and possessing a pathlength of 1 cm. Blanks were collected prior to each run and used to correct the data in the case of the solution measurements.

Raman Spectroscopy:

Raman data were collected on single crystals using a JASCO NRS-5500 Raman Spectrometer with a 532 nm laser. The Si substrate was used to calibrate the instrument. Single crystals of DBTTF and **1** were spread on a glass plate and placed on the instrument stage. The measurements were performed at the confocal mode with a 20x objective lens, 60 sec exposure time, and single accumulation on each compound. Other typical parameters used were: L1200/500 nm grating, 200×1000 μm slit, d-4000 μm aperture. Laser power was kept at 0.3 mW at 5% to avoid any sample decomposition during measurement. These data were collected on multiple crystals to eliminate any artifact possibility.

XANES Spectroscopy:

X-ray absorption near edge structure (XANES) data at the Ce L_{III} absorption edge were collected at the Stanford Synchrotron Radiation Lightsource (SSRL) beamline 11-2 using a Si (220) (φ = 0°) monochromator detuned to 50% and a Rh-coated harmonic rejection mirror with a cutoff energy set near 12 keV. The vertical slit height was sufficiently narrow that the energy resolution was core–hole lifetime limited. Data were collected in transmission geometry, and the monochromator energy was calibrated. Data were processed by subtracting a Chebyshev polynomial pre-edge background and normalizing the edge step to one. Powder samples were prepared in an argon-filled glovebox for measurement by mixing with dry boron nitride and packed into a slotted aluminum holder

with aluminized mylar windows, sealed with crushed indium wire. The sealed holders were kept under argon until measurement and exposed to air for less than one minute during transfer to vacuum. Samples were measured at 300 K using a liquid-helium cooled cryostat to test for temperature dependence of the resulting spectra. An easily oxidizable "canary" sample, such as cerium tris(tetramethylcyclopentadienyl) ($CeCp^{tet}_3$), was measured along with the samples to ensure that no O_2 had leaked into the sample holder during measurement. For representative plots of the standard and canary please see this reference.[2] The XANES spectrum of **1** was simulated using the FDMNES code to show that the fine structure in the edge does not arise from partial Ce(IV) character. A convolution over the density of states was calculated for a cluster with a 4 Å radius in multiple scattering mode using a Green's function method on a muffin-tin potential.

Magnetic Measurements:

Magnetic susceptibility and magnetization data were collected using a Quantum Design MPMS-7 SQUID magnetometer. Samples were prepared in a N_2 filled glovebox (Vacuum Atmospheres, Inc. Nexus II) under inert conditions. Polycrystalline sample of **1** was loaded into polyethylene bags using disposable spatulas to avoid impurities. Furthermore, ceramic forceps were used to handle the polybag to avoid direct touch of the glove with the loaded bag and these bags were subsequently sealed using a Ziploc v159 Vacuum Sealer System. The bags were then folded, inserted, and immobilized in a plastic drinking straw at specific length using disposable Q-tips and removed from the glovebox to mount in the SQUID magnetometer. Saturation magnetization measurements were performed at 2 K varying the applied field from 0 to 7 T. Magnetic susceptibility data were collected

at temperatures ranging from 2 to 300 K at an applied field of 2 T. Data were corrected for the diamagnetic contributions of the sample holder and bag by subtracting empty containers; corrections for the sample were calculated from Pascal's constants.

Photo-responsive DC magnetic moment measurements were collected in a Quantum Design MPMS XL 7 Tesla SQUID magnetometer using a Quantum Design Fiber-Optic Sample Holder (FOSH). Testing revealed that after removal of samples, some residual magnetism could be found on the holder. Solvent cleaning the holder was shown to reduce the residual moment to undetectable levels. All reported measurements were taken in the following manner: The FOSH was first cleaned and its background measured at all magnetic fields and temperatures used for sample measurements. The sample was then loaded and measurements collected. Finally, the raw data from the background measurements was subtracted from the sample measurements to reveal the net sample moment. Sample illumination was provided by the fiber-coupled output of a Coherent Verdi V5 laser system. Neutral density filters were used to reduce the output of the laser to the reported levels. Importantly, the empty FOSH holder showed no response to laser illumination. Due to the small sample volume and the inability to accurately determine the sample mass in the FOSH configuration, magnetic data are presented in terms of magnetic moment and relative magnetization changes rather than absolute molar quantities. All laser-ON and laser-OFF measurements were conducted on the same sample under identical conditions, ensuring internal consistency and direct comparability. In all cases, measurements were conducted under continuous 532 nm irradiation, and the light was switched off only after data acquisition to assess reversibility.

Transport Measurements:

Electrical transport data were obtained using a Keithley K236 Source-Measure Unit in a guarded two-probe measurement and a shielded, triaxial cable run straight from the K236 down a custom-made sample stick to the sample. Measurements were performed in a Quantum Design PPMS system, but the PPMS wiring was not used in the measurement. Final connections from the triaxial cable to the sample were made directly using gold wire, bypassing the PPMS "sample puck" wiring entirely. Crystals were not long enough to permit a four-wire measurement, however contact resistances is typically not a problem for such high resistance samples. Nevertheless, we performed additional measurements for the organic conductor TTF-TCNQ using the same contacts to assess the order of magnitude of contact resistance that might be expected. By comparing 2- and 4-wire measurements we find a contact resistance of ~10^2 Ohms, many orders of magnitude lower than the resistance values reported here. Photoconducting transients were induced using a 532 nm laser with computer-controlled power output and shutter, coupled to a multi-mode optical fiber that terminated approximately 1 mm above the sample. Given the f-number of the fiber, we estimate the maximum power density at the sample, denoted here as I_0, as 0.5 mW/mm^2, which is the same maximum power density used for the photo-magnetism measurements. Typical electrical transport data are shown in Figure S10-11. The increase in resistance at low temperature prevented us from measuring photoconducting transients below about 155 K. Photoconducting transients were measured at constant temperatures of 155 K, 160 K and 170 K by computer controlling the laser shutter. Data were recorded for 30 minutes of constant illumination

after stabilizing the sample resistance in the dark for 30 minutes. The main text shows examples of conductive transients for increasing power. In all cases, measurements were conducted under continuous 532 nm irradiation, and the light was switched off only after data acquisition to assess reversibility.

X-ray Structure Determination of Ce-DBTTF:

$C_{56}H_{32}Ce_2Cl_{10}S_{16}$, crystallizes in the monoclinic space group $P2_1/n$ (systematic absences 0k0: k=odd and h0l: h+l=odd) with a=13.8618(2)Å, b=15.5465(2)Å, c=15.6088(2)Å, β=109.663(2)°, V=3167.59(8)Å^3, Z=2, and d_{calc}=1.942 g/cm^3. X-ray intensity data were collected on a Rigaku XtaLAB Synergy-S diffractometer equipped with an HPC area detector (Dectris Pilatus3 R 200K) and employing confocal multilayer optic-monochromated Mo-Kα radiation (λ=0.71073 Å) at a temperature of 100K. Preliminary indexing was performed from a series of thirty 0.5° rotation frames with exposures of 5 seconds. A total of 1890 frames (12 runs) were collected employing ω scans with a crystal to detector distance of 50.0 mm, rotation widths of 0.5° and exposures of 35 seconds.
The crystal grew as a non-merohedral twin. The Ewald Explorer extension in CrysAlisPro[3] was used to index the diffraction images and to determine the twinning mechanism. Three components were able to be determined. The crystal was twinned by a rotation of 1.6° about the 0.0751 -0.9882 -0.1337 real direction and by a rotation of 178.6° about the 010 real direction. Rotation frames were integrated using CrysAlisPro[3], producing a listing of unaveraged F^2 and $\sigma(F^2)$ values. A total of 93145 reflections were measured over the ranges 4.82 ≤ 2θ ≤ 56.768°, -18 ≤ h ≤ 18, -20 ≤ k ≤ 20, -20 ≤ l ≤ 20 yielding 26461 unique reflections (R_{int} = 0.059). The intensity data were corrected for Lorentz and polarization

effects and for absorption using SCALE3 ABSPACK[4] (minimum and maximum transmission 0.9094, 1.0000). The structure was solved by dual space methods - SHELXT[5]. The $[Ce_2Cl_{10}]^{4-}$ complex lies on a crystallographic center of symmetry (at ½, ½,½). Thus the asymmetric unit consists of two TTF-derivative ions and ½ of a $[Ce_2Cl_{10}]^{4-}$ ion for a ratio of 4:1. Refinement was by full-matrix least squares based on F^2 using SHELXL[6]. All reflections were used during refinement. The weighting scheme used was $w=1/[\sigma^2(F_o^2)+ (0.0449P)^2 + 39.9883P]$ where $P = (F_o^2 + 2F_c^2)/3$. Non-hydrogen atoms were refined anisotropically and hydrogen atoms were refined using a riding model. Refinement converged to R1=0.0633 and wR2=0.1579 for 19599 observed reflections for which $F > 4\sigma(F)$ and R1=0.0889 and wR2=0.1703 and GOF =1.071 for all 26461 unique, non-zero reflections and 381 variables. The maximum Δ/σ in the final cycle of least squares was 0.001 and the two most prominent peaks in the final difference Fourier were +2.00 and -1.26 e/Å^3. The twinning parameters refined to a value of 0.2558(14), and 0.2025(13) respectively.

Synthetic Details for $(DBTTF)_4[Ce_2Cl_{10}]$

Photo-Crystallization: In aerobic conditions, to an oven-dried 20 mL scintillation vial charged with a Teflon-coated magnetic stir bar was added $CeCl_3$ (12.3 mg, 0.05 mmol, 1 equiv) and 4 mL EtOH, forming a clear colourless solution after 15 min stirring. To another 20 mL scintillation vial, DBTTF (30.5 mg, 0.10 mmol, 2 equiv) and a mixture of 6 mL $CHCl_3$, 5 mL CCl_4, and 5 mL CH_3CN were added with a Teflon-coated stir bar, forming a yellow solution after 15 min of stirring. The $CeCl_3$ solution was added to the DBTTF

solution, maintaining the yellow color. This solution was then irradiated (undisturbed) with a 370 nm Kessil lamp at 100% intensity, forming a dark green color immediately. After 3 h of irradiation, purple-black plates precipitated from the solution, leaving behind a yellow supernatant. Single crystals obtained from the reaction mixture were identified as $[DBTTF]_4[Ce_2Cl_{10}]$ (**1**) by X-ray diffraction. The bulk crystals were collected by filtration over a fine frit and dried under reduced pressure. Yield 17.0 mg, 0.009 mmol, 36.8%.

Anal. Calc. for $C_{56}H_{32}Ce_2Cl_{10}S_{16}$: C, 36.30; H, 1.74; Found: 36.61; 1.64

Control experiments described in the manuscript are summarized below in the table S1.

Control/Variation	Observation	Implication
No CCl_4	No precipitate, No DBTTF oxidation	Chloride radical originates from CCl_4
No Irradiation	No precipitate	Light essential to initiate photo-oxidation
No $CeCl_3$	Dark green solution, No precipitate,	[DBTTF]Cl soluble in solvent mixture
With $LaCl_3$	No precipitate	Process unique to Ce^{3+}
With $CeCl_3.7H_2O$	Crystals of **1** obtained	Hydration of salt doesn't affect reaction

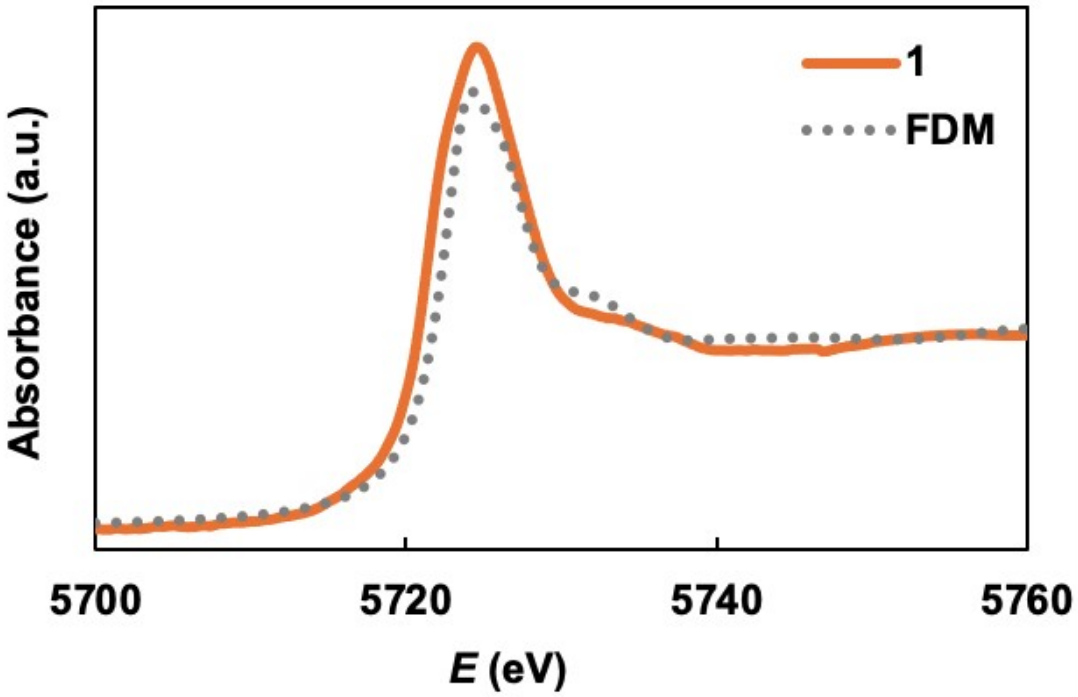

Figure S1: Ce L_{III}-edge XANES spectrum of **1** (solid orange), characteristic of formally Ce^{III} compounds, along with simulated data (dotted gray).

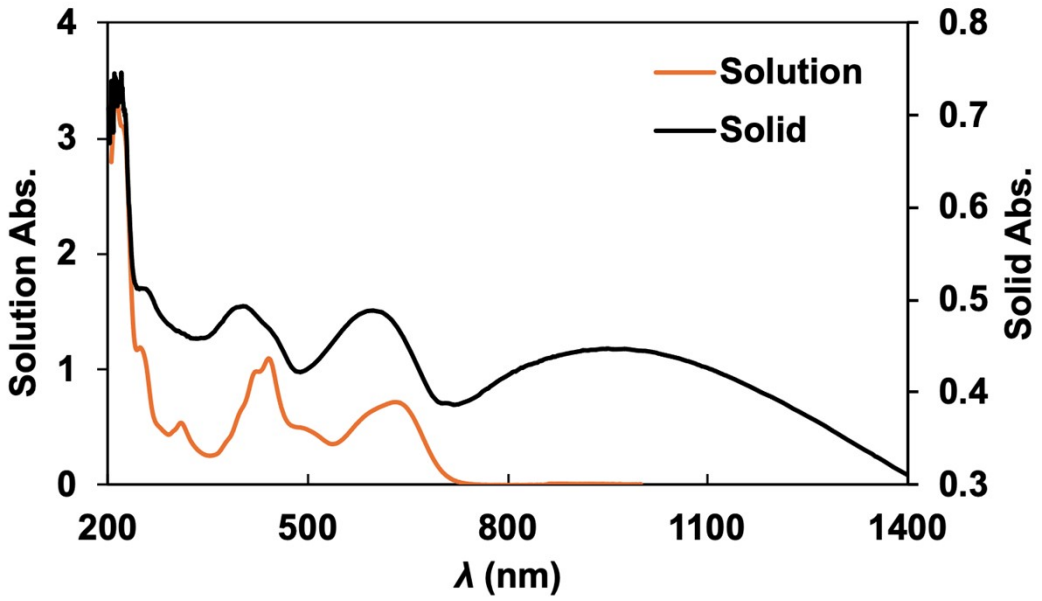

Figure S2: Electronic absorption spectroscopy data for **1** collected at room temperature in methanol (orange) and in the solid state (black). The solid-state data were collected in transmission mode on microcrystalline powder.

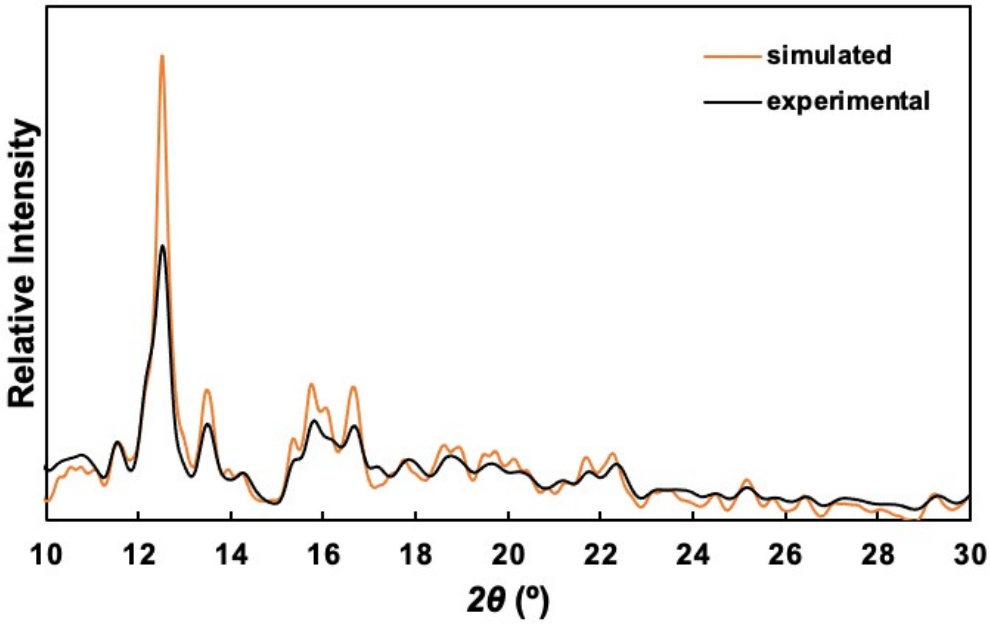

Figure S3: Powder pattern collected for **1** on bulk material (black). Powder pattern simulation generated from single crystal X-ray diffraction data (orange).

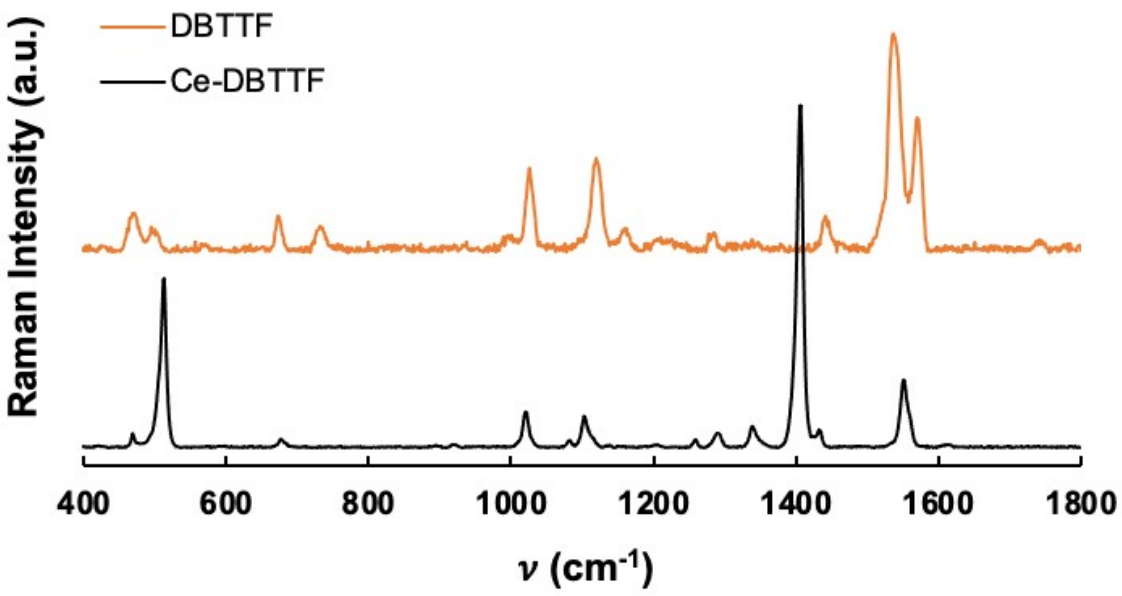

Figure S4: Raman data comparison for **1** (black) and DBTTF (orange) collected on single crystals.

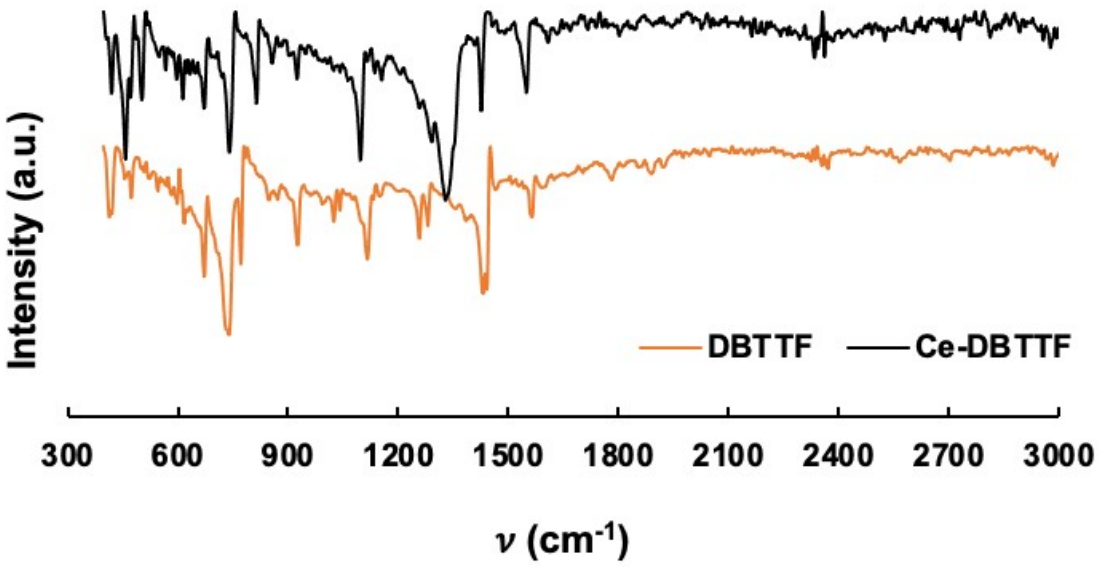

Figure S5: IR data comparison for **1** (black) and DBTTF (orange) collected in a KBr matrix.

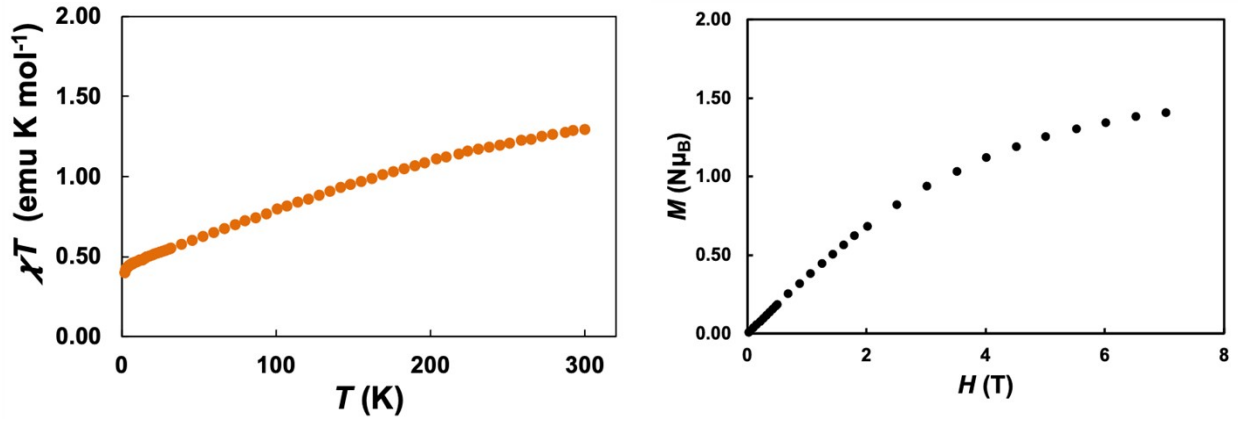

Figure S6: Variable temperature susceptibility measurement plots of **1** collected at 2 T (left). Magnetization saturation data for **1** collected at 2 K in the field range of 0-7 T (Right).

As shown below, the measured magnetic susceptibility for microcrystalline powder of **1** saturates sub-linearly with laser power. And the magnetization changes are a low-temperature phenomenon only occurring in **1** and not in the control sample $(NEt_4)_3[CeCl_6]$.

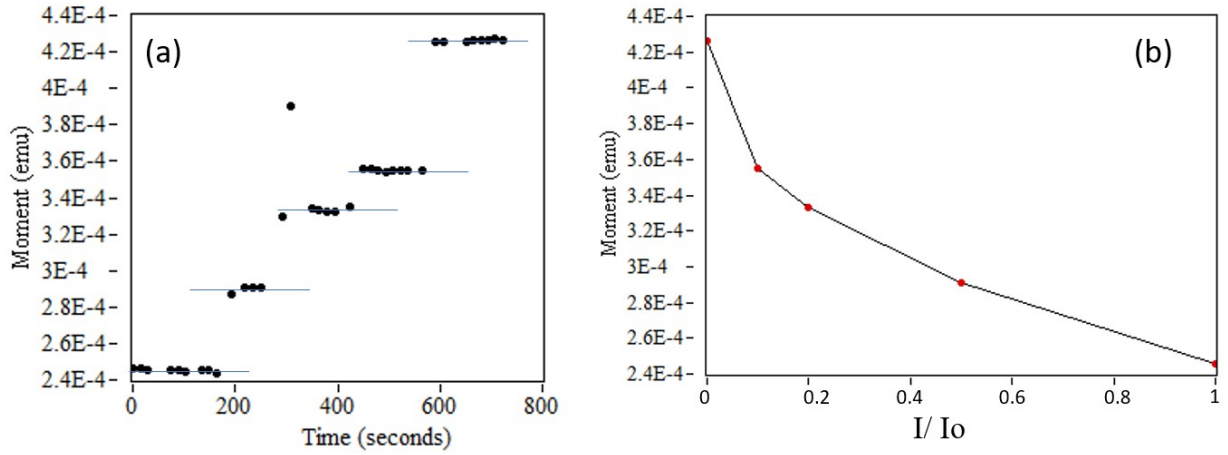

Figure S7: Power dependence of **1** moment recorded at T = 2K and B = 2 T. (a) Recorded magnetic moment in **1** versus time as optical power decreases, with straight lines added to show response plateaus. (b) Magnetic moment measured at these plateaus versus relative optical power.

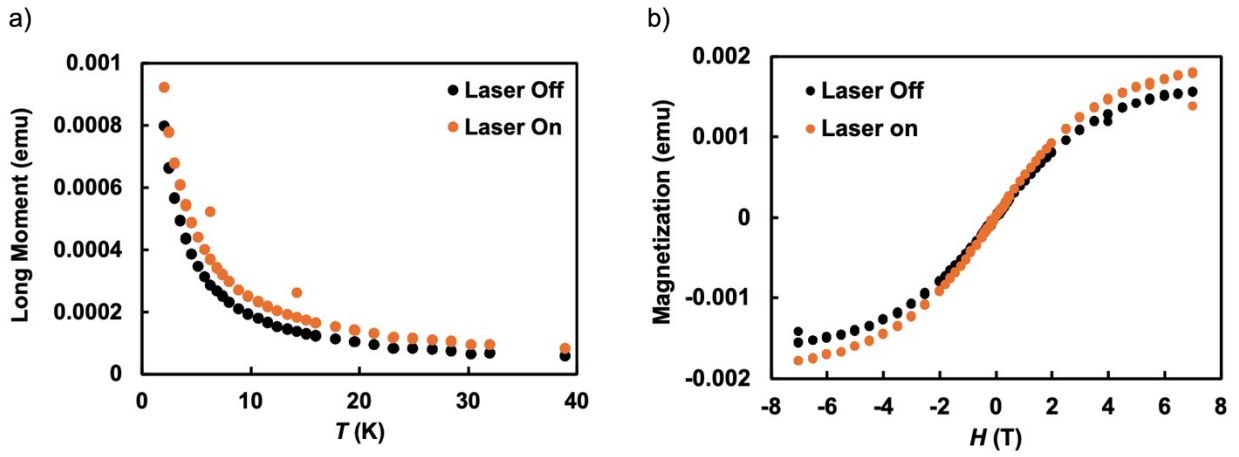

Figure S8: Temperature-dependent magnetization measured at 2 T for $(NEt_4)_3[CeCl_6]$. with laser off and laser on (I = Io). (b) Changes in magnetization with field for $(NEt_4)_3[CeCl_6]$ for the same laser irradiation used for Figure 4 in the main text.

The figures below show the mounting process for electrical transport measurements on single crystals of **1**. Samples are mounted on a thermally conducting but electrically insulating sapphire plate.

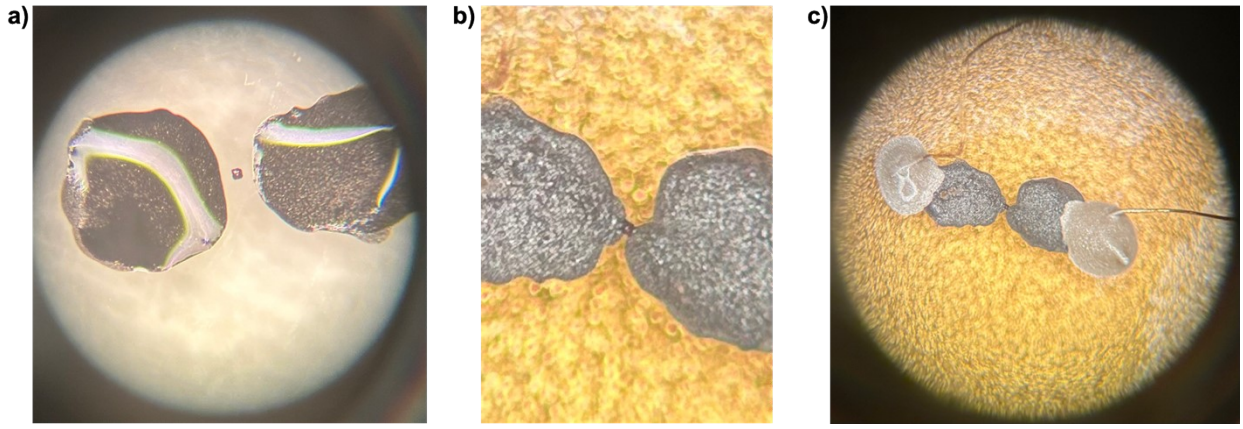

Figure S9: Crystal mounting process on the puck in pictures a) single crystal placed on a sapphire glass with two drops of carbon paste in each side of the crystal b) dried carbon paste connection made on each side of the crystal c) silver paste drops cast on each carbon paste spot, further connected with a gold wire.

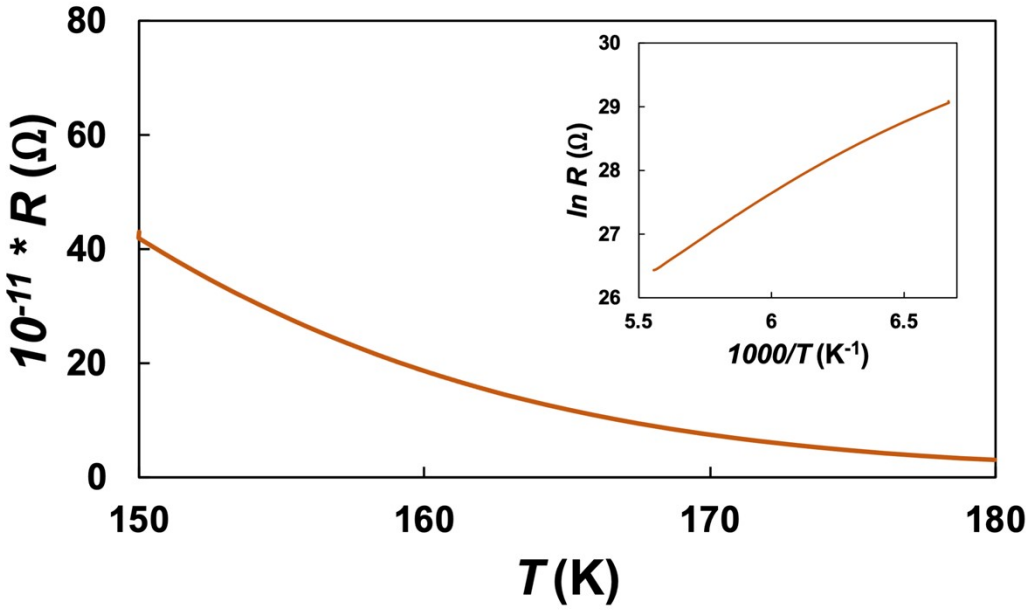

Figure S10: Temperature-dependent resistivity of single-crystal **1**. A subset of data was used to find the slope $\alpha \equiv dR/dT$ at 155 K, with a similar procedure used for 160 K and 170 K.

The power dependence of the maximum fractional resistive changes versus relative laser power was analyzed. One can see a sublinear relationship versus power. The sublinear dependence is already unusual if lattice heating is the source of the observed changes, however to test the idea that resistive changes arise from changes in temperature, we have converted the resistive changes, ΔR, to an effective temperature change, $\Delta R/\alpha$, shown in Figure S10 (b), where α is the slope dR/dT determined from R(T) (values of are -2.31e11 Ohms/K at 155 K, -1.64e11 Ohms/K at 160 K and -7.13e10 Ohms/K at 170 K).

There is no basis to suggest that laser-induced temperature changes would depend on sample temperature over this narrow range (155 K to 170 K); broad optical spectra cannot modulate absorption significantly over 6% change in temperature, and thermal conductivity of the sample and substrate will also vary slowly with temperature. Yet, there

is a large change in $\Delta R/\alpha$ from 160 K to 170 K. These data support that the quantity $\Delta R/\alpha$ does not report changes in sample temperature, and that heating is not solely the source of the photoconducting transients reported herein.

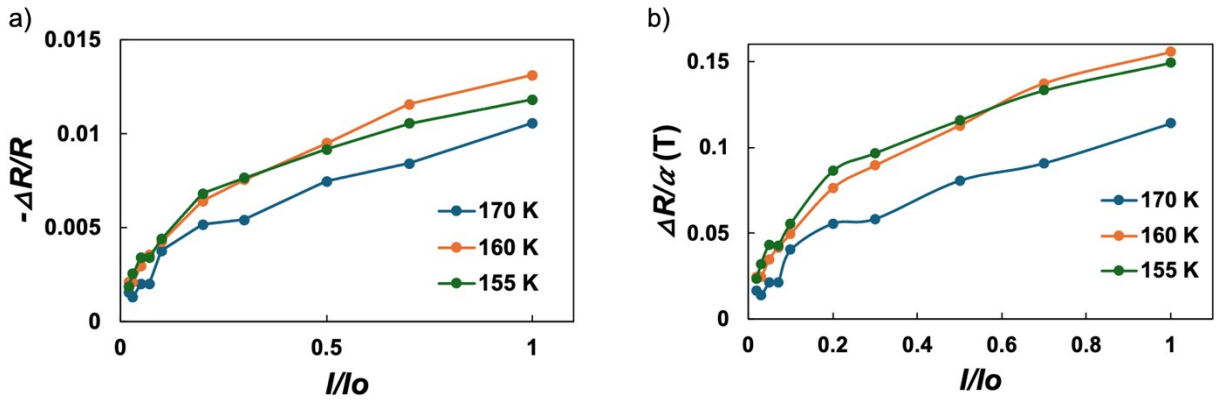

Figure S11: Power dependence of resistive changes on the single crystal of **1.** The points illustrate a subset of data used to find the slope $\alpha \equiv dR/dT$ at 155 K (-2.31e11 Ohms/K, green) green, 160 K (-1.64e11 Ohms/K, orange) and 170 K (-7.13e10 Ohms/K, blue).

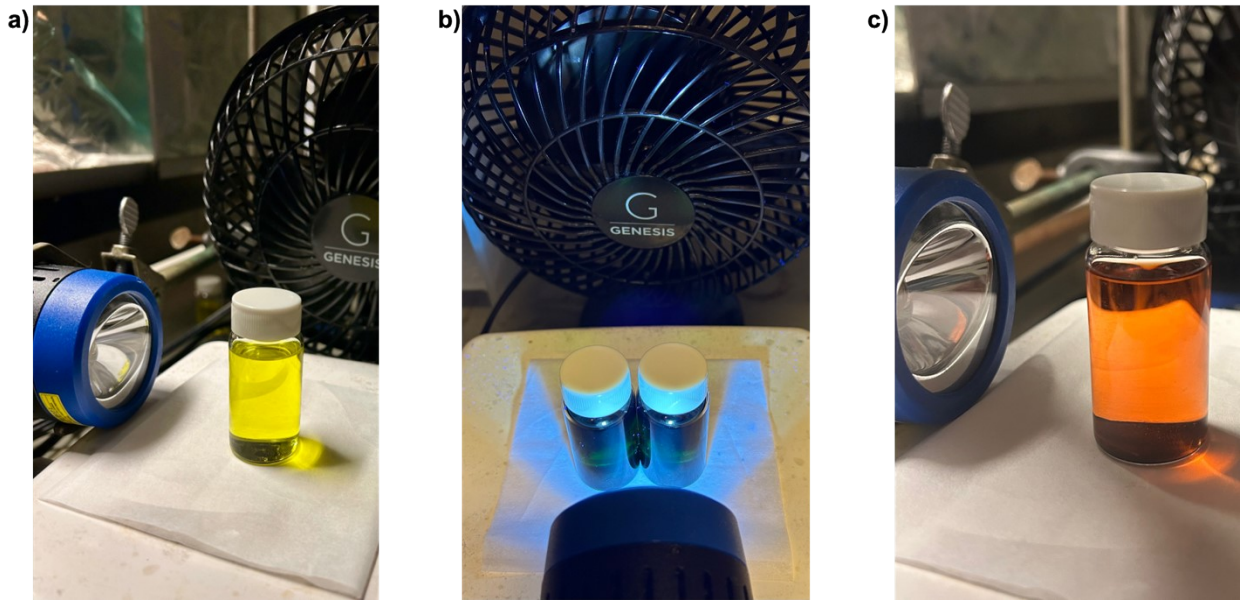

Figure S12: Photo-crystallization process in pictures a) Initial yellow solution before irradiation b) Dark green solution during irradiation c) Final solution with purple-black crystals of **1** at the bottom of the scintillation vial.

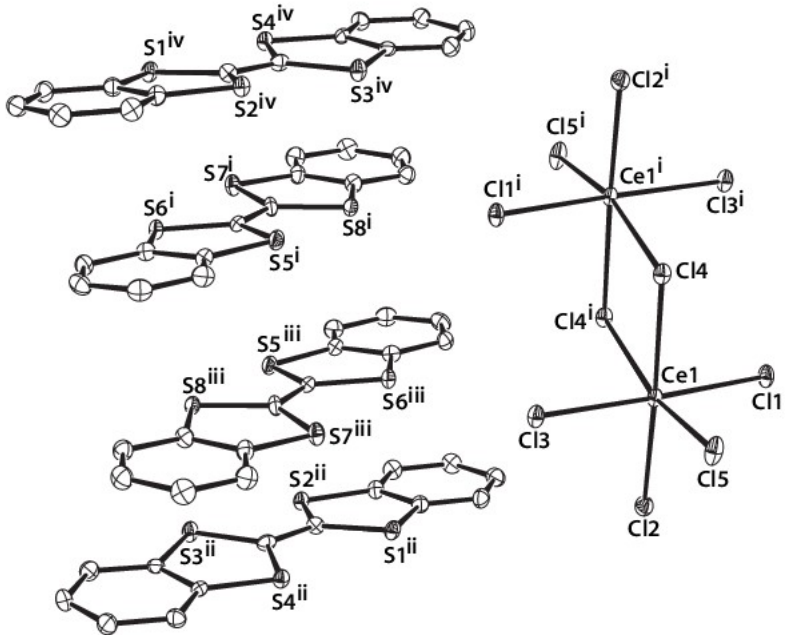

Figure S13: ORTEP drawing of **1** with 50% thermal ellipsoids (the primed atoms are symmetry generated).

Computational Details:

Periodic Calculations

Density functional theory (DFT) calculations were performed using the Vienna *ab-initio* Software Package (VASP) version 6.4.2 with the projector-augmented wave (PAW) method to describe the electron-ion interactions.[7, 8] All calculations were carried out using a plane wave cutoff of 550 eV on a Γ-only *k*-mesh. The H 1s, C 2s 2p, S 3s 3p, Cl 3s 3p and Ce 4f 5s 5p 5d 6s shells were treated explicitly. The electronic self-consistency threshold was set to 10^{-6} eV. The calculations began with the coordinates obtained via single-crystal X-ray diffraction, and only the hydrogen positions were optimized. These constrained optimizations employed the PBE[9] exchange-correlation (XC) functional, with van der Waals interactions described using the DFT-D3 method with a zero-damping function.[10, 11] A rotationally invariant Hubbard-U correction[12] of 5.0 eV was applied to the

Ce 4f-orbitals following a study of related Ce-containing materials.[13] This hydrogen-atom-position-optimized structure was employed for all further calculations.

The energies of two possible antiferromagnetic and one possible ferromagnetic collinear magnetic configurations of the Ce atoms were compared to determine the magnetic ground state at the PBE+U level of theory. One antiferromagnetic configuration aligned the magnetic moments of Ce atoms in each $Ce_2Cl_{10}^{4-}$ subunit and anti-aligned the moments between adjacent subunits. The second antiferromagnetic configuration anti-aligned the magnetic moments of Ce atoms within each subunit and aligned the magnetic moments between the shorter Ce-Ce pairs between adjacent subunits. The energies of all three configurations were found to be within less than 0.1 meV per atom of each other. The different magnetic states are nearly iso-energetic because the shortest distance between the $4f^1$ Ce ions is 4.49 Å within each $Ce_2Cl_{10}^{4-}$ unit and 11.23 Å between units, resulting in weak interactions between the Ce centers. The antiferromagnetic configuration that anti-aligned moments within Ce_2Cl_{10} subunits was chosen for further calculations.

TABLE S2: Magnetic moment of Ce atoms and electronic bandgap at the Γ-point for varying Hubbard-U parameters (PBE+U) vs. the HSE-06 screened hybrid functional for the antiferromagnetic configuration.

U value on Ce 4f (eV)	Magnetic Moment (μ_B) [a]	Band Gap (eV)
0	0.704	Metal

1	0.772	Metal
2	0.884	0.28
3	0.973	0.54
4	0.990	0.54
5	0.991	0.54
6	0.991	0.54
HSE-06	0.989	0.81

[a] Absolute Value

The optical absorption spectrum was calculated with the 'LOPTICS' functionality[14] in VASP, using both the PBE+U (U = 5 eV) and HSE-06 methods. Gaussian broadening of the peaks corresponded to sigma = 0.1 eV.

PBE+U calculations were performed where the effect of varying the U parameter on the magnetic moment and the band gap was evaluated. The data are collected in Table S2. For U chosen between 3 and 6 eV, the magnetic moment and band gap were essentially the same. Furthermore, the magnetic moment computed with the screened hybrid XC functional, HSE-06,[15, 16] was similar to that obtained with PBE+U (ca. ± 0.99) while the band gap increased from 0.54 eV to 0.81 eV. Note that for vanishing or small U, the system is predicted to be metallic (vanishing band gap). An opening of a band gap with the inclusion of either the Hubbard-U parameter or by including exact exchange in the screened hybrid functional is a hallmark of a Mott insulator.

Molecular Calculations

The molecular fragment of the DBTTF dimer was extracted from the experimental crystal structure. Full geometry optimizations were performed assuming a variety of different charges: $[DBTTF_2]^{q+}$ with q = 0 - 2. Each fragment charge combination underwent geometry optimization with the Amsterdam Density Functional Program Package.[17] The electron-electron interactions were described using the PBE functional with van der Waals interactions included via the DFT-D4 approximation.[18] An all-electron triple zeta basis with one polarization function (TZP) was employed, and spin-unrestricted optimizations were performed.

Additional calculations of the absorption spectrum of the DBTTF radical and a DBTTF dimer were performed using time-dependent DFT (TD-DFT) linear-response theory, as implemented in Gaussian 16.[18] A total of 100 and 200 excitations were computed for the monomer and dimer, respectively. These calculations utilized molecular structures extracted from the H-optimized crystal structure and were carried out to investigate whether the absorption spectrum is sensitive to the approximations in the XC functionals. Tested functionals included the non-hybrid functional PBE,[9] the hybrid functionals PBE0,[19] B3LYP,[20-22] and ωB97XD,[23] as well as the long-range-corrected functional CAM-B3LYP.[24] The def2-SVP and def2-SVPD basis sets were compared for the monomer to estimate potential errors from the basis set truncation;[25] however, the differences between calculated spectra obtained with the two basis sets were found to be insignificant. Solvent effects (methanol) were modeled using the conductor-like screening

model (COSMO).[26] In molecular geometry optimizations, dispersion interactions were accounted for using Grimme's D3 correction with Becke–Johnson (BJ) damping.[27]

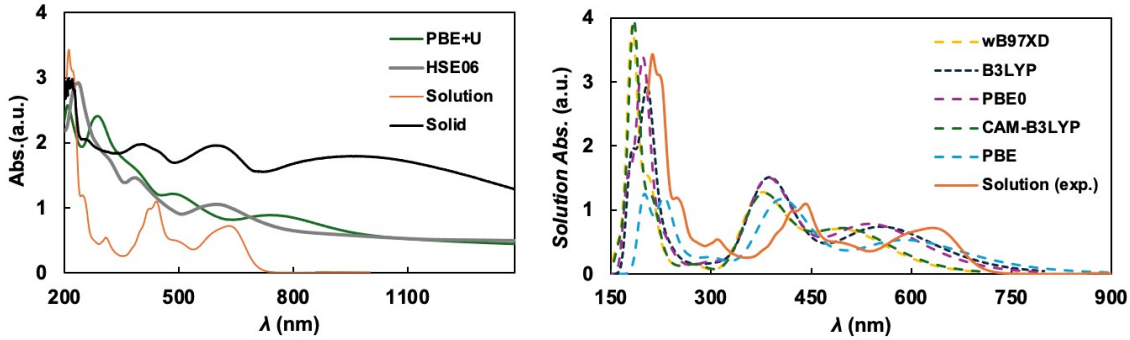

Figure S14: Absorption spectrum of $[DBTTF]_4[Ce_2Cl_{10}]$ calculated using different methods, (left) with PBC-DFT and (right) with molecular TD-DFT. The spectra have been arbitrarily scaled to lie on the same y-axis. Experimental solid-state and solution spectra are shown for comparison.

A key difference between the experimental spectra obtained in the solid state and in the solution phase is the presence of a broad tail at wavelengths above 700 nm in the former only. The lack of such a tail in the latter spectrum suggests that the tail results from excitations that are only available in the solid state. Both the HSE-06 and PBE+U calculations exhibit this tail, and are therefore consistent with the experiment, though the HSE-06 results appear to afford a somewhat better agreement with the data. Additional molecular calculations of absorption spectra were carried out for a $DBTTF^{\bullet+}$ monomer and a dimer thereof (Figure S14). First, it can be noted that the peak structure of the solution spectrum is rather well reproduced by the $DBTTF^{\bullet+}$ calculation, indicating that most of the absorption intensity seen in solution results from this species. Second, the calculations for the dimer, $(DBTTF^{\bullet+})_2$, likewise produce the peak structure seen experimentally below 700 nm for the solid, and they also produce a peak in the range of 800 to 900 nm. It therefore appears that much of the absorption measured for the solid of 1 is due to the singlet-coupled $(DBTTF^{\bullet+})_2$ moieties. Third, the calculated molecular

spectra do not display a strong dependence on the chosen functional, which is reassuring when considering that the solid-state calculations do not have a similar variety of available functionals. Fourth, however, the HSE-06 and PBE+U calculations clearly show that there are additional important contributions to the absorption intensity that result from the Ce(III) moieties.

Electronic Densities of States for the Solid

A comparison of the PBE+U and HSE-06 fragment-projected electronic density of states (PDOS) is provided in Figure S15. In the PBE+U PDOS, there are two sets of states near the Fermi level, and the band gap measures 0.54 eV. These states are mainly associated with the DBTTF moieties. The DOS from approximately 3 eV to 1.1 eV below the Fermi level (the latter being in the middle of the band gap) projects primarily onto the $[Ce_2Cl_{10}]^{4-}$ states, suggesting that photon energies between about 1.37 to 3.27 eV (380 to 905 nm) could excite electrons from the $[Ce_2Cl_{10}]^{4-}$ moieties to the DBTTF conduction states. With the HSE-06 XC functional, the band gap is increased to 0.81 eV and Ce states are also found to project onto the mainly DBTTF valence bands at about 0.405 eV below the Fermi energy, with significant character arising from the $[Ce_2Cl_{10}]^{4-}$ states to energies as low as 4 eV below the Fermi level. Thus, the HSE-06 band structure suggests that photons with energies between 0.81 to 4.405 eV (280 to 1530 nm) could excite electrons from $[Ce_2Cl_{10}]^{4-}$ to the DBTTF dimers.

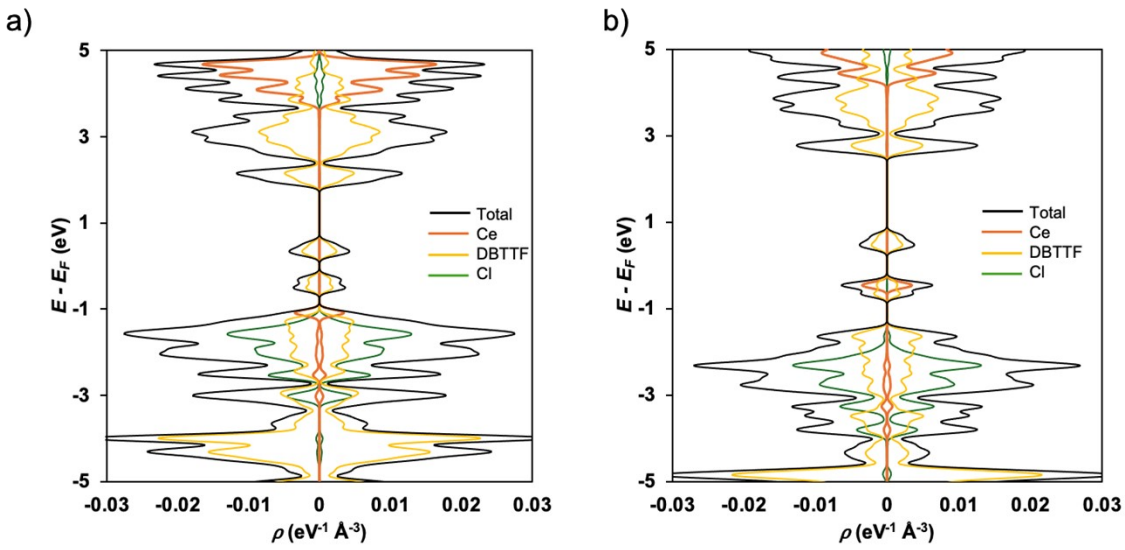

Figure S15: Total and species-projected electronic densities of states (DOS) for $[DBTTF]_4[Ce_2Cl_{10}]$ computed using the a) PBE+U and b) HSE-06 exchange-correlation functional. Positive and negative values of the DOS correspond to the spin-up and spin-down channels, respectively.

Another analysis tool used to determine the types of transitions that could occur upon irradiation is based on the joint densities of state (JDOS)[28] plotted in Figure 4. This approach counts the number of possible transitions to any unoccupied state that could occur for a particular photon energy (wavelength), without considering the transition probabilities. The PBE+U JDOS suggests that a photon with an energy greater than 1.36 eV can cause a $[Ce_2Cl_{10}]^{4-} \rightarrow [DBTTF]_2^{2+}$ electronic transition, while within HSE-06 such transitions are allowed between 0.81 to 1.09 eV, and above ~2.1 eV.

In the experiments, $[DBTTF]_4[Ce_2Cl_{10}]$ was excited with λ = 532 nm (2.33 eV) light. At this wavelength, both the PBE+U and HSE06 JDOSs predict that excitations from Ce_2Cl_{10} into DBTTF unoccupied bands can occur.

Molecular Geometries of the DBTTF Dimer

The distances between the central C-C atoms in the $[DBTTF]_2^{2+}$ molecular fragment relaxed with the ADF package measured 1.397 Å, in good agreement with the experimental bond distances of 1.396 and 1.405 Å in the solid. In the ADF-optimized system the distances between the midpoints of the C-C bonds in the nearly planar DBTTF molecules comprising the $[DBTTF]_2^{2+}$ dimer were found to be 3.365 Å, as compared to the 3.26(1) Å measured between the stacked molecular units in the solid. The good agreement between the central C bond distances and the distance between the stacked DBTTF molecules obtained from the X-ray crystal diffraction and computed for the $[DBTTF]_2^{2+}$ molecular fragment provides further evidence of the strong π-dimer formation in the synthesized compound.

The highest occupied molecular orbital (HOMO) computed for $[DBTTF]_2^{2+}$ was σ bonding between the molecular orbitals of π symmetry on each $DBTTF^{\cdot+}$ molecule, with significant overlap of the orbitals on the central C and S atoms (Figure S16), resembling the HOMO computed for the +2 charged π-stacked TTF dimer [14].[29] The lowest unoccupied orbital (LUMO) of both $[DBTTF]_2^{2+}$ and $[TTF]_2^{2+}$ represents the antibonding combination of these same two p-type molecular orbitals; filling it would be expected to destabilize the dimer, leading to an increase of the distance between the two molecules.

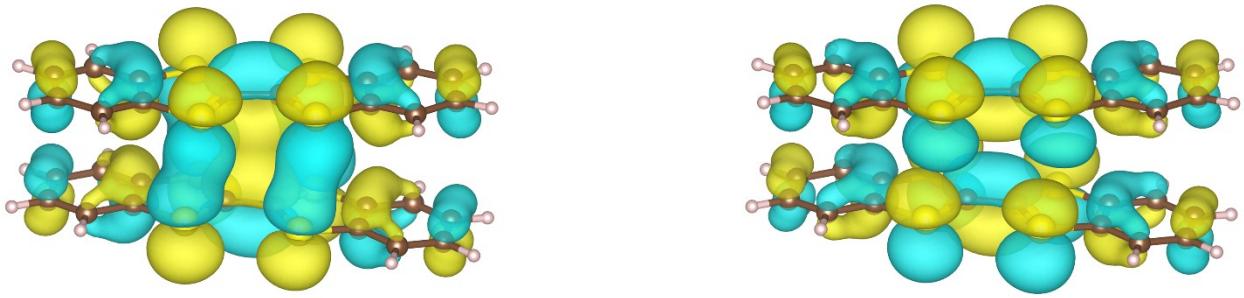

Figure S16: The highest occupied molecular orbital (HOMO) and lowest unoccupied molecular orbital (LUMO) computed for the $[DBTTF]_2^{2+}$ dimer (isovalue = 0.016).

Coordinates of H-Optimized $[DBTTF]_4[Ce_2Cl_{10}]$ Crystal Structure (VASP Format)

Ce4 H64 C112 S32 Cl20

1.00000000000000

13.0534912050869778 0.0000000000000000 -4.6643184495397509

-0.0000000000000010 15.5465000000000000 0.0000000000000010

0.0000000000000000 0.0000000000000000 15.6088000000000005

Ce H C S Cl

4 64 112 32 20

Direct

0.36095 0.47908 0.54054

0.13905 0.97908 0.95946

0.63905 0.52092 0.45946

0.86095 0.02092 0.04054

0.357502347 0.153306736 0.062632875

0.142497697 0.653306741 0.437367129

0.642497671 0.846693341 0.937367076

0.857502285 0.346693335 0.562632919

0.376289082 0.087622338 0.209903478

0.123711007 0.587622341 0.290096567

0.623710937 0.912377656 0.790096464

0.876288979 0.412377653 0.70990349

0.401709871 0.17988221 0.347746852

0.098290203 0.679882223 0.152253153

0.598290156 0.82011783 0.652253169

0.901709785 0.320117817 0.847746829

0.411359516 0.337015758 0.338753851

0.088640545 0.837015761 0.161246166

0.588640508 0.662984215 0.661246164

0.911359442 0.162984212 0.838753821

0.372447489 0.799301226 0.007047073

0.127552573 0.299301227 0.492952949

0.627552503 0.200698874 0.992952854

0.872447422 0.700698875 0.507047122

0.366357844 0.864308278 0.862016765

0.133642209 0.364308272 0.637983246

0.633642147 0.135691711 0.137983127

0.866357794 0.635691716 0.362016864

0.360325135 0.770748948 0.728691301

0.13967497 0.270749201 0.771308626

0.639674859 0.229251057 0.271308699

0.860325036 0.729250806 0.228691372

0.357292423 0.613403338 0.740452153

0.142707562 0.11340335 0.759547848

0.642707575 0.386596686 0.259547825

0.857292431 0.886596674 0.240452171

0.333286858 0.939925731 0.199770103

0.166713217 0.439925709 0.300229925

0.666713147 0.060074267 0.800229901

0.833286785 0.560074291 0.699770069

0.338082045 0.795501976 0.142253477

0.161918166 0.295501958 0.357746556

0.66191795 0.204498059 0.85774652

0.83808185 0.704498074 0.642253449

0.367230826 0.667086933 0.243822833

0.132769282 0.16708693 0.256177194

0.632769169 0.332913053 0.756177189

0.867230731 0.832913058 0.743822791

0.386758999 0.684576864 0.406555121

0.113241087 0.184576857 0.093444904

0.613241023 0.315423222 0.593444997

0.886758897 0.815423233 0.906554972

0.402457785 0.013755457 0.861377773

0.097542301 0.513755464 0.638622243

0.597542228 0.986244495 0.138622172

0.902457691 0.486244485 0.361377816

0.405321133 0.157906715 0.925444309

0.094678959 0.657906704 0.574555715

0.594678874 0.842093328 0.074555692

0.905321037 0.342093341 0.425444284

0.396348389 0.28870001 0.829419303

0.103651684 0.788700012 0.670580718

0.603651617 0.71130001 0.170580652

0.896348314 0.211300009 0.329419331

0.384030482 0.274980446 0.668700134

0.115969554 0.774980448 0.831299862

0.615969572 0.725019581 0.331299918

0.884030432 0.225019581 0.168700095

0.374 0.4389 0.063

0.126 0.9389 0.437

0.626 0.5611 0.937

0.874 0.0611 0.563

0.3747 0.2828 0.1174

0.1253 0.7828 0.3826

0.6253 0.7172 0.8826

0.8747	0.2172	0.6174
0.3708	0.1939	0.1224
0.1292	0.6939	0.3776
0.6292	0.8061	0.8776
0.8708	0.3061	0.6224
0.3807	0.1574	0.2058
0.1193	0.6574	0.2942
0.6193	0.8426	0.7942
0.8807	0.3426	0.7058
0.3949	0.2089	0.2824
0.1051	0.7089	0.2176
0.6051	0.7911	0.7176
0.8949	0.2911	0.7824
0.4001	0.2979	0.2783
0.0999	0.7979	0.2217
0.5999	0.7021	0.7217
0.9001	0.2021	0.7783
0.3889	0.335	0.1944
0.1111	0.835	0.3056
0.6111	0.665	0.8056
0.8889	0.165	0.6944
0.3709	0.5131	0.0118
0.1291	0.0131	0.4882

0.6291	0.4869	0.9882
0.8709	0.9869	0.5118
0.3711	0.6685	0.9567
0.1289	0.1685	0.5433
0.6289	0.3315	0.0433
0.8711	0.8315	0.4567
0.3713	0.758	0.9503
0.1287	0.258	0.5497
0.6287	0.242	0.0497
0.8713	0.742	0.4503
0.3681	0.7945	0.8679
0.1319	0.2945	0.6321
0.6319	0.2055	0.1321
0.8681	0.7055	0.3679
0.3635	0.7423	0.7934
0.1365	0.2423	0.7066
0.6365	0.2577	0.2066
0.8635	0.7577	0.2934
0.3621	0.6532	0.7992
0.1379	0.1532	0.7008
0.6379	0.3468	0.2008
0.8621	0.8468	0.2992
0.3663	0.6161	0.8816

0.1337	0.1161	0.6184
0.6337	0.3839	0.1184
0.8663	0.8839	0.3816
0.3742	0.9535	0.4956
0.1258	0.4535	0.0044
0.6258	0.0465	0.5044
0.8742	0.5465	0.9956
0.3583	0.8948	0.338
0.1417	0.3948	0.162
0.6417	0.1052	0.662
0.8583	0.6052	0.838
0.3454	0.8852	0.2458
0.1546	0.3852	0.2542
0.6546	0.1148	0.7542
0.8454	0.6148	0.7458
0.3496	0.8033	0.2144
0.1504	0.3033	0.2856
0.6504	0.1967	0.7856
0.8496	0.6967	0.7144
0.3639	0.7314	0.2704
0.1361	0.2314	0.2296
0.6361	0.2686	0.7296
0.8639	0.7686	0.7704

0.3754	0.7402	0.3619
0.1246	0.2402	0.1381
0.6246	0.2598	0.6381
0.8754	0.7598	0.8619
0.3717	0.8227	0.3955
0.1283	0.3227	0.1045
0.6283	0.1773	0.6045
0.8717	0.6773	0.8955
0.3792	0.0065	0.5699
0.1208	0.5065	0.9301
0.6208	0.9935	0.4301
0.8792	0.4935	0.0699
0.3916	0.0625	0.7277
0.1084	0.5625	0.7723
0.6084	0.9375	0.2723
0.8916	0.4375	0.2277
0.399	0.0701	0.819
0.101	0.5701	0.681
0.601	0.9299	0.181
0.899	0.4299	0.319
0.4005	0.1518	0.8546
0.0995	0.6518	0.6454
0.5995	0.8482	0.1454

0.9005	0.3482	0.3546
0.3956	0.2244	0.8013
0.1044	0.7244	0.6987
0.6044	0.7756	0.1987
0.8956	0.2756	0.3013
0.3884	0.2179	0.7102
0.1116	0.7179	0.7898
0.6116	0.7821	0.2898
0.8884	0.2821	0.2102
0.3865	0.1361	0.6741
0.1135	0.6361	0.8259
0.6135	0.8639	0.3259
0.8865	0.3639	0.1741

0.36071	0.33747	0.01634
0.13929	0.83747	0.48366
0.63929	0.66253	0.98366
0.86071	0.16253	0.51634
0.39473	0.44529	0.17812
0.10527	0.94529	0.32188
0.60527	0.55471	0.82188
0.89473	0.05471	0.67812
0.37331	0.61436	0.05549
0.12669	0.11436	0.44451

0.62669 0.38564 0.94451

0.87331 0.88564 0.55549

0.36584 0.50527 0.8999

0.13416 0.00527 0.6001

0.63416 0.49473 0.1001

0.86584 0.99473 0.3999

0.35572 0.99446 0.38882

0.14428 0.49446 0.11118

0.64428 0.00554 0.61118

0.85572 0.50554 0.88882

0.38621 0.84384 0.50889

0.11379 0.34384 0.99111

0.61379 0.15616 0.49111

0.88621 0.65616 0.00889

0.3857 0.96391 0.67332

0.1143 0.46391 0.82668

0.6143 0.03609 0.32668

0.8857 0.53609 0.17332

0.3786 0.11675 0.56096

0.1214 0.61675 0.93904

0.6214 0.88325 0.43904

0.8786 0.38325 0.06096

0.36886 0.30942 0.4973

0.13114 0.80942 0.0027

0.63114 0.69058 0.5027

0.86886 0.19058 0.9973

0.1538 0.47736 0.46436

0.3462 0.97736 0.03564

0.8462 0.52264 0.53564

0.6538 0.02264 0.96436

0.35131 0.65138 0.5693

0.14869 0.15138 0.9307

0.64869 0.34862 0.4307

0.85131 0.84862 0.0693

0.58377 0.48601 0.61618

0.91623 0.98601 0.88382

0.41623 0.51399 0.38382

0.08377 0.01399 0.11618

0.36135 0.44094 0.70959

0.13865 0.94094 0.79041

0.63865 0.55906 0.29041

0.86135 0.05906 0.20959

Table S3. Summary of Structure Determination of 1

Empirical formula	$C_{56}H_{32}Ce_2Cl_{10}S_{16}$
Formula weight	1852.51
Diffractometer	Rigaku XtaLAB Synergy-S (Dectris Pilatus3 R 200K)
Temperature/K	100
Crystal system	monoclinic
Space group	$P2_1/n$
a	13.8618(2)Å
b	15.5465(2)Å
c	15.6088(2)Å
β	109.663(2)°
Volume	3167.59(8)Å^3
Z	2
d_{calc}	1.942 g/cm^3
μ	2.409 mm^{-1}
F(000)	1820.0
Crystal size, mm	0.08 × 0.06 × 0.05
2θ range for data collection	4.82 - 56.768°
Index ranges	-18 ≤ h ≤ 18, -20 ≤ k ≤ 20, -20 ≤ l ≤ 20
Reflections collected	93145
Independent reflections	26461[R(int) = 0.059]
Data/restraints/parameters	26461/0/381
Goodness-of-fit on F^2	1.071
Final R indexes [I>=2σ (I)]	R_1 = 0.0633, wR_2 = 0.1579
Final R indexes [all data]	R_1 = 0.0889, wR_2 = 0.1703
Largest diff. peak/hole	2.00/-1.26 eÅ^{-3}

(1) Yin, H.; Jin, Y.; Hertzog, J. E.; Mullane, K. C.; Carroll, P. J.; Manor, B. C.; Anna, J. M.; Schelter, E. J. The Hexachlorocerate(III) Anion: A Potent, Benchtop Stable, and Readily Available Ultraviolet A Photosensitizer for Aryl Chlorides. *Journal of the American Chemical Society* **2016**, *138* (50), 16266-16273. DOI: 10.1021/jacs.6b05712.
(2) Moreau, L. M.; Lapsheva, E.; Amaro-Estrada, J. I.; Gau, M. R.; Carroll, P. J.; Manor, B. C.; Qiao, Y.; Yang, Q.; Lukens, W. W.; Sokaras, D.; Schelter, E. J.; Maron, L.; Booth, C. H. Electronic structure studies reveal 4f/5d mixing and its effect on bonding characteristics in Ce-imido and -oxo complexes. *Chemical Science* **2022**, *13* (6), 1759-1773, 10.1039/D1SC06623D. DOI: 10.1039/D1SC06623D.
(3) CrysAlisPro 1.171.42.101a. Rigaku Oxford Diffraction, Rigaku Corporation: Oxford, UK, 2023.
(4) SCALE3 ABSPACK v1.0.7: an Oxford Diffraction program. Oxford Diffraction Ltd: Abingdon, UK, 2005.
(5) Sheldrick, G. M. SHELXT v2018/2. Acta Cryst., A, 71, 3-8: **2015**.
(6) Sheldrick, G. M. SHELXL-2019/3. Acta Cryst., A, 71, 3-8 **2015**.
(7) Kresse, G.; Furthmüller, J. Efficient iterative schemes for ab initio total-energy calculations using a plane-wave basis set. *Physical Review B* **1996**, *54* (16), 11169-11186. DOI: 10.1103/PhysRevB.54.11169.
(8) Kresse, G.; Joubert, D. From ultrasoft pseudopotentials to the projector augmented-wave method. *Physical Review B* **1999**, *59* (3), 1758-1775. DOI: 10.1103/PhysRevB.59.1758.
(9) Perdew, J. P.; Burke, K.; Ernzerhof, M. Generalized Gradient Approximation Made Simple. *Physical Review Letters* **1996**, *77* (18), 3865-3868. DOI: 10.1103/PhysRevLett.77.3865.
(10) Grimme, S. Semiempirical GGA-type density functional constructed with a long-range dispersion correction. *Journal of Computational Chemistry* **2006**, *27* (15), 1787-1799. DOI: https://doi.org/10.1002/jcc.20495.
(11) Grimme, S.; Antony, J.; Ehrlich, S.; Krieg, H. A consistent and accurate ab initio parametrization of density functional dispersion correction (DFT-D) for the 94 elements H-Pu. *The Journal of Chemical Physics* **2010**, *132* (15). DOI: 10.1063/1.3382344 .
(12) Dudarev, S. L.; Botton, G. A.; Savrasov, S. Y.; Humphreys, C. J.; Sutton, A. P. Electron-energy-loss spectra and the structural stability of nickel oxide: An LSDA+U study. *Physical Review B* **1998**, *57* (3), 1505-1509. DOI: 10.1103/PhysRevB.57.1505.
(13) Pandey, P.; Wang, X.; Gupta, H.; Smith, P. W.; Lapsheva, E.; Carroll, P. J.; Bacon, A. M.; Booth, C. H.; Minasian, S. G.; Autschbach, J.; Zurek, E.; Schelter, E. J. Realization of Organocerium-Based Fullerene Molecular Materials Showing Mott Insulator-Type Behavior. *ACS Applied Materials & Interfaces* **2024**, *16* (14), 17857-17869. DOI: 10.1021/acsami.3c18766.
(14) Gajdoš, M.; Hummer, K.; Kresse, G.; Furthmüller, J.; Bechstedt, F. Linear optical properties in the projector-augmented wave methodology. *Physical Review B* **2006**, *73* (4), 045112. DOI: 10.1103/PhysRevB.73.045112.
(15) Heyd, J.; Scuseria, G. E.; Ernzerhof, M. Hybrid functionals based on a screened Coulomb potential. *The Journal of Chemical Physics* **2003**, *118* (18), 8207-8215. DOI: 10.1063/1.1564060.
(16) Krukau, A. V.; Vydrov, O. A.; Izmaylov, A. F.; Scuseria, G. E. Influence of the exchange screening parameter on the performance of screened hybrid functionals. *The Journal of Chemical Physics* **2006**, *125* (22). DOI: 10.1063/1.2404663.
(17) te Velde, G.; Bickelhaupt, F. M.; Baerends, E. J.; Fonseca Guerra, C.; van Gisbergen, S. J. A.; Snijders, J. G.; Ziegler, T. Chemistry with ADF. *Journal of Computational Chemistry* **2001**, *22* (9), 931-967. DOI: https://doi.org/10.1002/jcc.1056.
(18) *Gaussian 16 Rev. C.01*; Wallingford, CT, 2016.
(19) Adamo, C.; Barone, V. Toward reliable density functional methods without adjustable parameters: The PBE0 model. *The Journal of Chemical Physics* **1999**, *110* (13), 6158-6170. DOI: 10.1063/1.478522.
(20) Becke, A. D. Density-functional thermochemistry. III. The role of exact exchange. *The Journal of Chemical Physics* **1993**, *98* (7), 5648-5652. DOI: 10.1063/1.464913.

(21) Becke, A. D. Density-functional exchange-energy approximation with correct asymptotic behavior. *Physical Review A* **1988**, *38* (6), 3098-3100. DOI: 10.1103/PhysRevA.38.3098.
(22) Lee, C.; Yang, W.; Parr, R. G. Development of the Colle-Salvetti correlation-energy formula into a functional of the electron density. *Physical Review B* **1988**, *37* (2), 785-789. DOI: 10.1103/PhysRevB.37.785.
(23) Chai, J.-D.; Head-Gordon, M. Long-range corrected hybrid density functionals with damped atom–atom dispersion corrections. *Physical Chemistry Chemical Physics* **2008**, *10* (44), 6615-6620, 10.1039/B810189B. DOI: 10.1039/B810189B.
(24) Yanai, T.; Tew, D. P.; Handy, N. C. A new hybrid exchange–correlation functional using the Coulomb-attenuating method (CAM-B3LYP). *Chemical Physics Letters* **2004**, *393* (1), 51-57. DOI: https://doi.org/10.1016/j.cplett.2004.06.011.
(25) Weigend, F.; Ahlrichs, R. Balanced basis sets of split valence, triple zeta valence and quadruple zeta valence quality for H to Rn: Design and assessment of accuracy. *Physical Chemistry Chemical Physics* **2005**, *7* (18), 3297-3305, 10.1039/B508541A. DOI: 10.1039/B508541A.
(26) Pye, C. C.; Ziegler, T. An implementation of the conductor-like screening model of solvation within the Amsterdam density functional package. *Theoretical Chemistry Accounts* **1999**, *101* (6), 396-408. DOI: 10.1007/s002140050457.
(27) Grimme, S.; Ehrlich, S.; Goerigk, L. Effect of the damping function in dispersion corrected density functional theory. *Journal of Computational Chemistry* **2011**, *32* (7), 1456-1465. DOI: https://doi.org/10.1002/jcc.21759.
(28) Orapunt, F.; O'Leary, S. K. Spectral variations in the optical transition matrix element and their impact on the optical properties associated with hydrogenated amorphous silicon. *Solid State Communications* **2011**, *151* (5), 411-414. DOI: https://doi.org/10.1016/j.ssc.2010.11.026.
(29) Garcia-Yoldi, I.; Miller, J. S.; Novoa, J. J. Theoretical Study of the Electronic Structure of [Tetrathiafulvalene]22+ Dimers and Their Long, Intradimer Multicenter Bonding in Solution and the Solid State. *The Journal of Physical Chemistry A* **2009**, *113* (2), 484-492. DOI: 10.1021/jp807022h.